J. Fluid Mech. (1984), *vol.* 138, *pp.* 1–19
Printed in Great Britain

Measurements near a laminar separation point

By R. L. VARTY AND I. G. CURRIE
Department of Mechanical Engineering, University of Toronto, Ontario

(Received 12 August 1982 and in revised form 6 April 1983)

Measurements in the neighbourhood of a laminar separation point at a high subcritical Reynolds number are reported. These results are used to test the validity of various theories relating to laminar separation. It is concluded that the boundary-layer equations are valid in the neighbourhood of the separation point without the existence of a singularity.

The velocity field was measured using a dual-beam laser-Doppler anemometer with optical frequency shifting. The wall-shear-stress distribution was measured with a flush-mounted hot-film sensor and the wall-pressure distribution was measured using a strain-gauge pressure sensor. The various terms in the Navier–Stokes equations were evaluated directly from the measurements, permitting the validity of the boundary-layer equations to be established. Proposed solutions for the flow field are compared with the measured flow field.

1. Introduction

Separation is the dominant feature of many high-Reynolds-number laminar flows. The difficulty of solving the Navier–Stokes equations for separated flows has led to the solution of simplified problems. The most common simplification is the use of the boundary-layer equations in place of the complete Navier–Stokes equations. Both the simplifications and the resulting solutions may be tested by measuring separated flows.

The class of flows considered here have bounding surfaces which are neither streamlined nor have sharp edges. The flow is steady, laminar and two-dimensional and the fluid is incompressible. Furthermore, the boundary layer which develops on the wall is laminar and well established. For example, this class of flows would include a circular cylinder in a flow field for which the Reynolds number is in the range 10^3–10^5.

In solving the boundary-layer equations, the pressure or velocity at the edge of the boundary layer may be specified as a boundary condition. This boundary condition represents the effect of the external flow field upon the boundary layer. However, the external flow is influenced by the presence of the boundary layer whose solution is sought; therefore the external flow is not known beforehand. If the pressure or velocity at the edge of the boundary layer is arbitrarily assumed, the resulting solution of the boundary-layer equations is singular at the separation point. Moreover, the singularity persists when an experimental pressure distribution is expressed mathematically and used as a boundary condition. Extensive reviews of this and other matters relating to laminar separation have been made by Brown & Stewartson (1969) and by Williams (1977). The existence of such a singularity indicates that either the boundary-layer equations or the boundary condition have no physical basis in the neighbourhood of the separation point.

Alternative boundary conditions have been found which allow solutions to the

boundary-layer equations that are not singular at the separation point (see Williams 1977). In such 'inverse solutions', a specified quantity such as the displacement thickness of the boundary layer or the wall shear stress has a given distribution which is finite and continuous at the separation point. The corresponding pressure or velocity at the edge of the boundary layer is then deduced from the solution.

The purpose of the present paper is to present measurements obtained in the neighbourhood of a laminar separation point so as to establish the physical relevance of the mathematics.

2. Apparatus and procedure

2.1. *Design*

The experiment was designed to measure the flow in the neighbourhood of a separation point. This region of the flow extends slightly beyond the boundary-layer thickness at separation δ_s, and is centred on the separation point. This region includes some of the development of the near-wall flow on either side of the separation point and includes part of the external flow near the edge of the boundary layer.

A circular cylinder followed by a long splitter plate was chosen as the bluff body. The splitter plate was used to prevent the periodic vortex shedding which would otherwise occur, thus ensuring a steady flow. The dimensions of the cylinder and of the splitter plate are shown in figure 1.

A relatively large cylinder diameter was chosen to permit measurements of high spatial resolution in the neighbourhood of the separation point. Water was used as a working fluid because preliminary tests showed that naturally occurring dust particles in the water supply were of a suitable type and number to scatter laser light efficiently. The provision of an adequate number of scattering particles in the boundary layer of an air flow proved to be difficult without seriously disturbing the flow.

The test section shown in figure 1 was used for the experiment. The size of the measuring volume of the laser-Doppler anemometer (LDA) increases with the focal length of the optical system, placing an upper limit on the depth of the test section if acceptable spatial resolution is to be obtained. This led to a test cylinder of small aspect ratio. The practical upper limit on the flow rate and the lower limit on the freestream velocity placed an upper limit on the height of the test section. This resulted in a test section with a blockage ratio of 37 %. These limits on the height and width of the test section prevent direct comparison of the measurements with results for much longer cylinders in more extensive flow fields. Nonetheless, a suitable separated flow is obtained and the neighbourhood of the separation point can be accurately measured. It is assumed that the applicability of the boundary-layer equations is independent of the blockage ratio.

The measuring techniques used were non-invasive, accurate, and as independent of any flow model as possible. The small size of the neighbourhood of the separation point and the marginal stability of the flow there require the use of techniques that do not disturb the flow. The small size of the separation region requires techniques that provide high spatial resolution. Establishing whether time-dependent phenomena were present dictated techniques that could detect rapid changes in the flow. The measurement of small flow quantities and their derivatives required techniques of high accuracy. Since the understanding of separated flow is incomplete, the interpretation of measurements should be as independent of flow models as possible, and should avoid assumptions about the nature of the separation-region flow. These

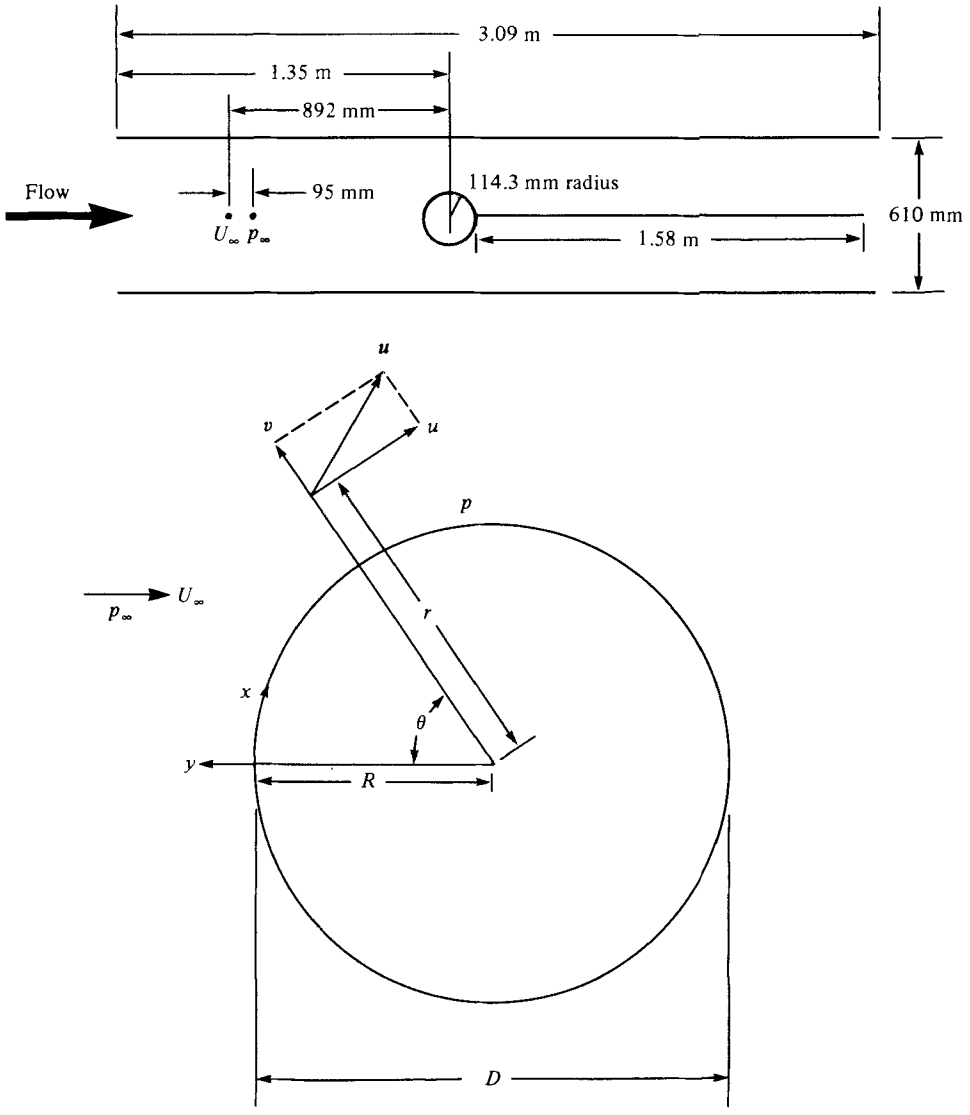

FIGURE 1. Side view of the test section. The model consists of a circular cylinder followed by a splitter plate. The depth of the test section is 203 mm. The other internal dimensions of the test section are shown.

criteria were satisfied using an LDA to measure velocity, a flush-mounted hot-film sensor to measure wall shear stress and a differential pressure transducer of the strain-gauge type to measure wall pressure.

2.2. *Coordinate systems and notation*

The coordinate systems are defined with the aid of figure 1. The primary coordinate system is the wall coordinate system (x, y) with its origin at the front of the cylinder. The secondary coordinate system is the polar coordinate system (r, θ) with its origin at the centre of the cylinder. In both coordinate systems, the velocity $\boldsymbol{u}$ is resolved into a tangential velocity component u and a radial velocity component v. The pressure is denoted by p.

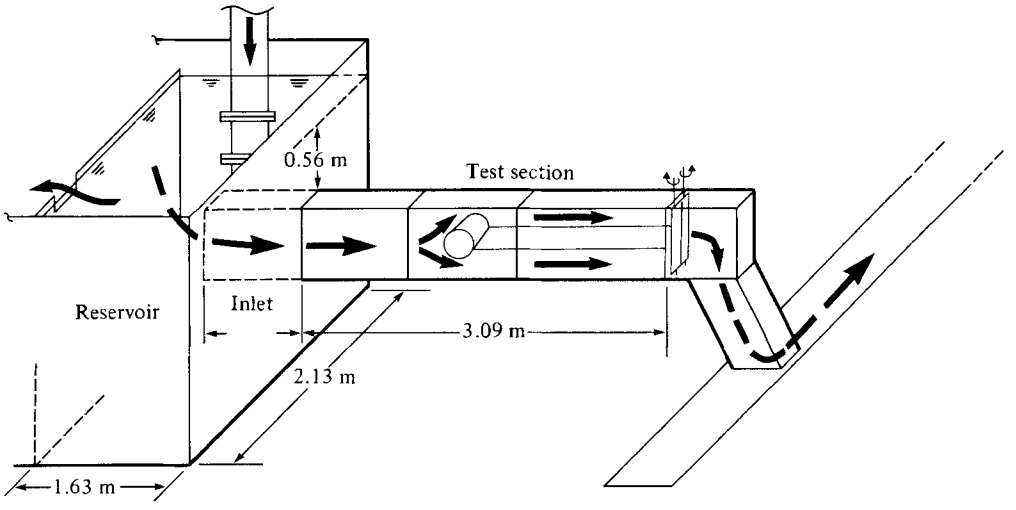

FIGURE 2. Water tunnel. The test-section flow is supplied by a constant-head reservoir.

The general scheme of subscripts and superscripts is as follows. Quantities in the incident freestream have the subscript ∞ and are measured well upstream of the cylinder. The freestream velocity U_∞ and the freestream pressure are measured at slightly different positions to avoid interference of the velocity and pressure sensors. Quantities measured at the wall have the subscript w, and are functions of x alone. The subscript s identifies the value of a quantity at the separation point. Dimensionless variables are identified by the superscript $*$ and are formed from their dimensional counterparts using the cylinder radius R as the characteristic length, the freestream velocity U_∞ as the characteristic velocity and the quantity ρU_∞^2 as the characteristic pressure, where ρ is the density of the fluid.

The Reynolds number, based on the cylinder diameter, is $Re_D = U_\infty D/\nu$, where ν is the kinematic viscosity of the fluid.

2.3. *Water tunnel*

The water tunnel is shown in figure 2. The headbox of an existing flume was modified to serve as a constant-head reservoir for the water tunnel. The water entered the tunnel through an inlet section within the reservoir which was equipped with a curved mouth, turbulence-reducing screens and a honeycomb to encourage parallel flow. The working section had clear Plexiglas walls supported by an external aluminium frame. Drainage from the tunnel was recirculated via the channel system of the laboratory using a propeller-type pump. A dual butterfly valve at the end of the tunnel was used to control the flowrate.

The cylinder, splitter plate and test section are shown in figure 1. The cylinder was a Plexiglas tube machined to an outside diameter of 228.6 ± 0.06 mm and a surface roughness average, as measured by a Talysurf 10, of 0.2 μm. The cylinder spanned the centre of the test section and was mounted on a sealed shaft through the sidewalls of the tunnel. The cylinder could be rotated about its axis with an accuracy of $\pm 0.1°$. The test section was 610 mm high and 203 mm wide. The gap between the end of the cylinder and the wall was less than 1 mm. A 1.58 m long splitter plate was placed downstream of the cylinder and spanned the width of the test section. The small clearance between the plate and cylinder was sealed using pliable weather-stripping foam glued to the end of the plate.

All measurements were made at the midspan of the cylinder.

2.4. *Laser-Doppler anemometer*

The tangential velocity u in the separation region and the freestream velocity U_∞ were measured using separate dual-beam forward-scatter LDA optical systems. Each system used a helium–neon laser emitting a 632.8 μm wavelength light beam. A 15 mW laser was used in the u optical system and a 5 mW laser was used in the U_∞ optical system. The optical components were manufactured by Opto-Elektronische Instrumente GmbH & Co. (OEI) and Thermo-Systems Inc. (TSI). Both systems shared a single TSI 1090 frequency-tracker signal-processor so that u and U_∞ could not be measured simultaneously.

The u-optical system was equipped with dual Bragg-cell frequency shifting, enabling forward flow to be distinguished from reverse flow and permitting the tracker to process small and fluctuating velocities accurately.

The u transmitting optics were mounted in a special traversing mechanism which allowed the measuring volume to be moved along radial lines and circular arcs. This motion was achieved by a carriage which was rotated about a shaft collinear with the cylinder axis and within which the transmitting optics were moved radially along straight, threaded shafts. Since the LDA velocity reading is independent of the position of the receiving optics, it was possible to realign the receiving optics manually without the aid of a similar traversing mechanism. The $y = 0$ point was established by reference to the surface of the cylinder at its ends. It was estimated that an error of ± 0.13 mm in the y-position was possible. This uncertainty was about $\frac{1}{30}$ of the boundary-layer thickness. The estimated uncertainty in the distance from the nominal $y = 0$ position to any other y-position was ± 0.08 mm.

A measure of the half-width of the measuring volume in a given direction is the standard deviation of the irradiance distribution in that direction. For the u LDA system, $\sigma_x \approx \sigma_y \approx 54$ μm. In comparison, the boundary-layer thickness at separation δ_s was about 3 mm, so that $2\sigma_y/\delta_s \approx \frac{1}{30}$.

In measuring the tangential velocity component u, the plane defined by the two laser beams was parallel to a plane tangent to the cylinder. The components of velocity in other directions can be measured by rotating the plane defined by the laser beams. The angle of rotation relative to the tangential plane is limited by the requirement that the beams do not intersect the surface of the cylinder. The permitted angle of rotation increases from 0 at the cylinder surface to about 30° at the edge of the boundary layer. In view of this limited angle and the expectation that $v \ll u$, an indirect measurement of v by this means was considered to be inherently inaccurate. Instead, v was obtained from u using the equation of continuity.

2.5. *Hot-film shear-stress sensor*

The wall shear stress τ_w was measured by a flush-mounted hot-film sensor because this was more accurate than differentiation of the measured tangential velocity u with respect to the distance from the wall y.

A TSI 1268W hot-film sensor was used. It consisted of a rectangular platinum thin film deposited on a cylindrical quartz substrate. This was mounted with the sensor flush to the surface using the technique described by Tillman & Schlieper (1979*a*). The streamwise length of the sensor was 0.12 mm and its spanwise width was 1 mm. The diameter of the substrate was 1.5 mm.

The sensor was installed at the midspan position of the cylinder and was calibrated before being placed in the water tunnel. This cylinder was placed at rest inside a rotating cylinder and the space between them was filled with water, forming a circular Couette flow. Such a flow has already been used by Tillman & Schlieper (1979*b*) for

calibrating such a sensor. This configuration avoids any centrifugal instability of the laminar flow, and the Reynolds number of the flow was small enough to ensure laminar, rather than turbulent, flow.

The calibration data were fitted to the response equation

$$E_A^2 = H_1 \tau_w^{\frac{1}{3}} + H_0,$$

where E_A is the voltage output of the constant-temperature anemometer connected to the hot-film sensor. The dependence of H_1 and H_0 on temperature was established to provide accurate measurements during water temperature changes of about 1 °C in the water tunnel.

The main disadvantage of the hot-film sensor was its insensitivity to the direction of the wall shear stress. This was overcome by using the LDA data to help interpret the hot-film data.

2.6. *Pressure transducer*

A Viatran 223 differential pressure transducer, using a strain gauge to measure the deformation of a diaphragm subjected to a pressure difference, was used to measure the difference $p_\infty - p_w$ between the freestream pressure and the wall pressure. The characteristic dynamic pressure of the water tunnel system was $\frac{1}{2}\rho U_\infty^2 = 23.1$ Pa $= 2.4$ mmH_2O, which is quite small. The need to measure the small pressures and the need for small size ruled out commercially available flush-mounting pressure sensors. The pressure transducer was calibrated using the known pressure difference between two open tanks of water. It was then connected to the water tunnel flow via 5 mm bore plastic tubes and 1 mm diameter pressure taps.

2.7. *Data acquisition*

The electrical signals produced by the LDA, hot-film sensor and pressure transducer were fed into a PDP-11/03 digital computer via an analog-to-digital interface. The computer was programmed to convert the digitized signals into instantaneous velocity, shear stress and pressure values and to analyse these values.

In order to detect any unsteadiness in the flow and to provide statistically stable mean values, signals were sampled at a rate of 40 Hz for 1 min intervals.

3. Results of the experiment

3.1. *Flow validation*

A Reynolds number $Re_D = (4.68 \pm 0.26) \times 10^4$ was obtained by operating the water tunnel at a freestream velocity of $U_\infty = 0.215 \pm 0.005$ m/s and a temperature of 17.9 ± 1.2 °C. The uncertainty in these quantities results mainly from limitations in controlling the velocity and temperature rather than from measurement uncertainty.

The freestream velocity was uniform within 4 %, had a turbulence intensity of 3.2 % and a turbulence integral scale of 52 mm. Since the integral scale of the freestream turbulence is much larger than the boundary-layer thickness, a turbulent boundary layer should not be induced by freestream turbulence.

The flow in the separation region was visualized by injecting an aqueous solution of potassium permanganate into the wake of the cylinder through a 1 mm diameter hole in the cylinder at midspan and $\theta = 100°$. The dye darkened the region of recirculating flow so that the separation streamline, which bounds the recirculating flow, could be located. The line of separation had a locus defined by $\theta \approx 81.5° \pm 0.5°$ except within about 20 mm of the sidewalls of the tunnel, where the tunnel boundary

layer affected the flow past the cylinder. The predominant motion of the dye was in the plane perpendicular to the axis of the cylinder. The motion of the dye and the constancy of the line of separation along the span of the cylinder demonstrated that the flow was steady and two-dimensional.

3.2. *Uncorrected measurements*

Velocity profiles were obtained from $\theta = 75°$ to 89° for increments of 0.5° near the separation point and 1.0° increments further away. Some representative, uncorrected velocity profiles are shown in figure 3. The velocity has been made dimensionless using $u^* = u/U_\infty$ and the distance from the wall has been made dimensionless using $y^* = y/R$. Both the mean velocity, denoted by mean (u^*) and the standard deviation of the velocity, denoted by sd (u^*), are shown in figure 3.

It may be assumed that mean values are being considered unless indicated otherwise. For example, u^* would usually refer to the mean velocity, and its occasional use to represent instantaneous velocity would be clearly stated.

The wall-shear-stress distribution was measured from $\theta = 75°$ to 89° for increments of 0.5° near the separation point and 1.0° increments further away. The uncorrected wall-shear-stress distribution is shown in figure 4. The dimensionless wall-shear-stress coefficient $C_\tau = \tau_w/(\frac{1}{2}\rho U_\infty^2)$ has been plotted.

The wall-pressure distribution was measured from $\theta = 75°$ to 89° for increments of 0.5° near the separation point and 1.0° increments further away. The uncorrected wall-pressure distribution is shown in figure 5. The dimensionless wall-pressure coefficient $C_p = (p_w - p_\infty)/(\frac{1}{2}\rho U_\infty^2)$ has been plotted.

Reliable average values and measures of their reproducibility were obtained by repeating each measurement at least once. The velocity was measured at each position of interest and then the entire set of velocity measurements was repeated once. Wall-shear-stress and wall-pressure measurements were made at each position and then the entire set of shear-stress or pressure measurements was repeated five times.

3.3. *Corrected measurements*

Velocity-gradient broadening, caused by the variation of velocity across the LDA measuring volume, produced biased readings of mean (u) and sd (u). The corrections for this effect were estimated by the technique of Durst, Melling & Whitelaw (1976). The correction to mean (u) was neglected because it was much smaller than the instrument uncertainty. The correction to sd (u) was also negligible, except near $\theta = 75°$, where $\partial u/\partial y$ is large.

The values of $\partial u^*/\partial y^*$ used in the corrections for velocity gradient broadening, and the values of other derivatives of the velocity used later, were calculated as follows. A uniform rectangular mesh, with spacing about the same size as the experimental data, was constructed. The values of u^* at the mesh points were obtained from 2-dimensional linear interpolation on the data, since the data did not form a regular mesh. Local smoothing was applied in the x^* direction. Derivatives in the x^* and y^* directions were calculated by standard second-order finite-difference formulas at interior points and first-order formulas at boundary points.

Some differences between the wall shear stress calculated from the LDA velocity measurements and that measured directly using the hot-film sensor were apparent. In contrast to the LDA readings, the hot-film readings were positive for $\theta > \theta_s$, and non-zero for $\theta = \theta_s$. These differences resulted from the insensitivity of the hot-film sensor to the direction of the wall shear stress, an effect called rectification. This effect

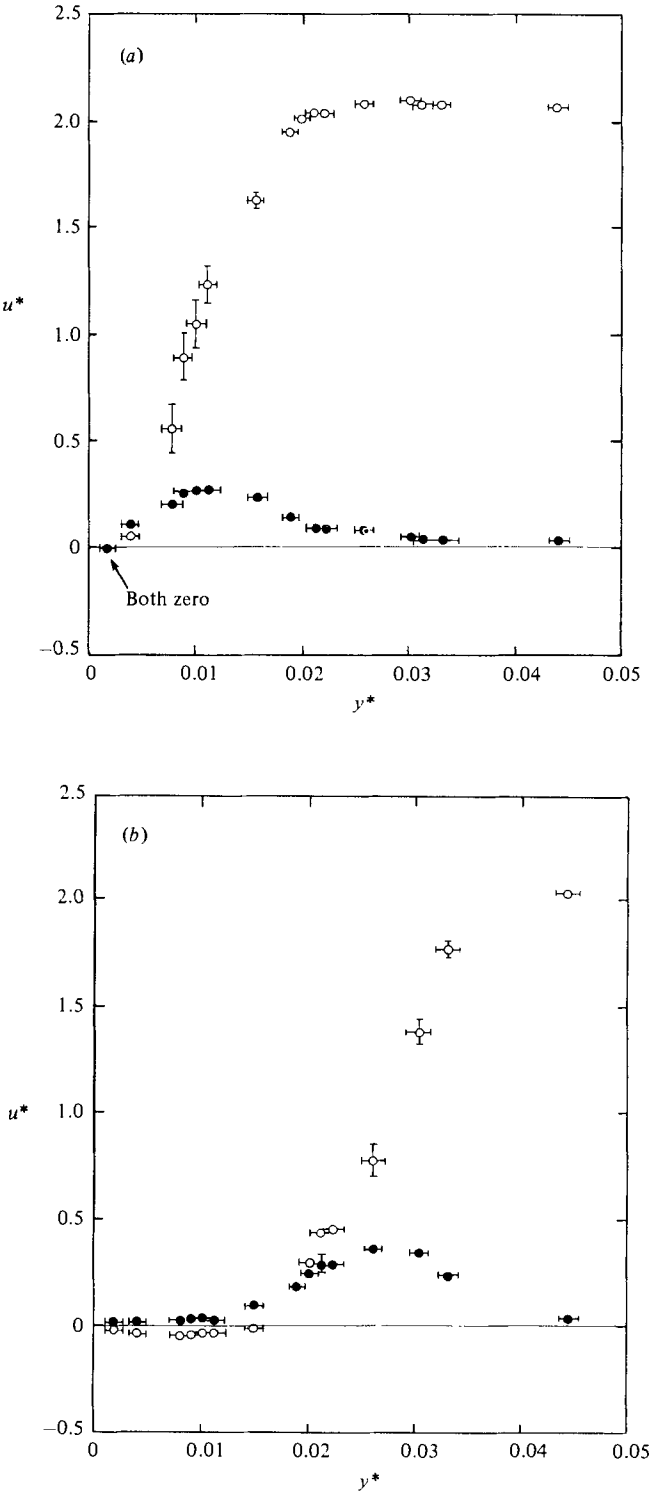

FIGURE 3. Velocity data obtained with the LDA: ○, mean velocity; ●, standard deviation of velocity. (*a*) $\theta = 81.5°$; (*b*) $\theta = 89.0°$.

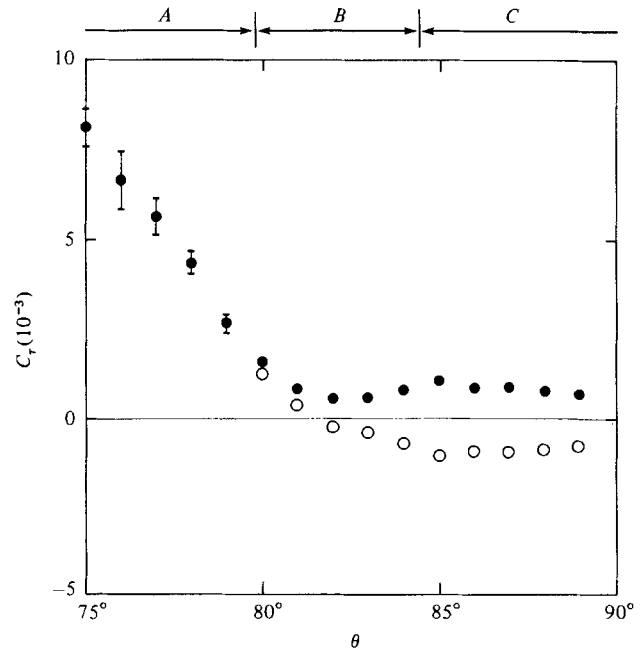

FIGURE 4. Wall-shear-stress data obtained with the hot-film sensor: ●, uncorrected; ○, corrected. Three regions exist: *A*, complete forward flow; *B*, mixed forward and reverse flow; *C*, complete reverse flow.

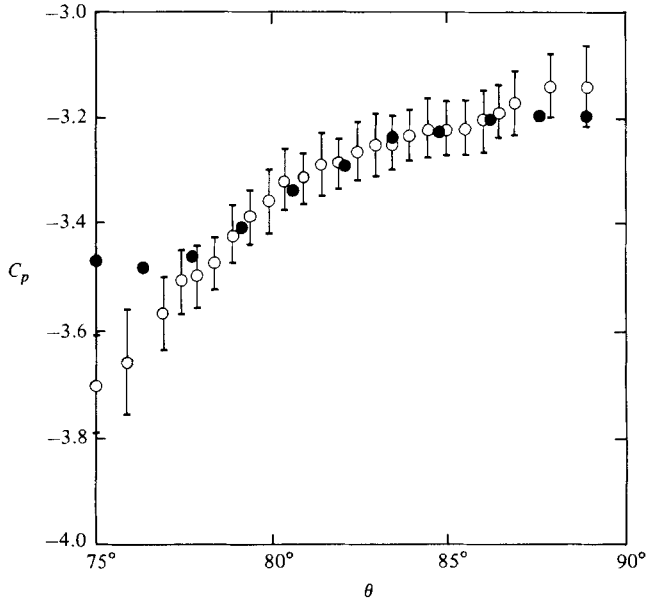

FIGURE 5. Comparison of pressure distributions: ○, measured with the pressure transducer; ●, calculated from the velocity measurements.

caused positive readings for $\theta > \theta_s$ even though τ_w was actually negative, and when combined with the slight unsteadiness of the flow, caused a positive reading for $\theta = \theta_s$ even though τ_w was actually 0. The divergence of the results near $\theta = 75°$ was caused by the substantial uncertainty in measuring y^*, and hence calculating $\partial u^*/\partial y^*$, by the LDA approach. Because of this uncertainty, the hot-film measurements were considered to be more accurate than the LDA measurements, even though the hot-film measurements suffered from the rectification effect.

The hot-film measurements were corrected for rectification by comparing the probability density functions of the instantaneous readings of the hot-film sensor and the LDA. The thermal boundary-layer thickness of the hot-film sensor was estimated to be 0.3 mm. The LDA readings nearest the wall were at $t = 0.2 \pm 0.1$ mm and the width of the LDA measuring volume in the y-direction was about 0.05 mm. Therefore the hot-film sensor and the LDA data obtained nearest the wall measured approximately the same part of the flow field. The wall shear stress was proportional to the velocity gradient $\partial u/\partial y$ at the wall. Unfortunately, the velocity gradient could not be accurately calculated because of the large uncertainty in position. Thus, the constant of proportionality between the wall shear stress and the velocity reading nearest the wall could not be accurately inferred from the measured position of the velocity measurement. Instead, the probability density functions of the hot-film sensor and the LDA data obtained nearest the wall were plotted. The close similarity of their shapes indicated that both instruments measured the same part of the flow field. The required constant of proportionality was deduced from the ratio of standard deviations of the two functions and then applied to yield the corrected wall shear-stress distribution shown in figure 4.

It was not necessary to correct the pressure distribution shown in figure 5.

4. Analysis of the experimental data

4.1. *Kinematics*

The distributions of boundary-layer thickness δ^*, displacement thickness δ_1^* and momentum thickness δ_2^* are shown in figure 6. The boundary-layer thickness was defined by

$$\delta^*(x^*) = y^* \quad \text{such that} \quad u^*(x^*, y^*) = 0.99 U^*(x^*),$$

and the velocity of the external flow U^* was defined by

$$U^*(x^*) = \max_{y^* > 0} (u^*(x^*, y^*)).$$

The displacement thickness was defined by

$$\delta_1^* = \int_0^\infty \left(1 - \frac{u^*}{U^*}\right) \mathrm{d}y^*,$$

and the momentum thickness was defined by

$$\delta_2^* = \int_0^\infty \frac{u^*}{U^*}\left(1 - \frac{u^*}{U^*}\right) \mathrm{d}y^*.$$

The radial velocity component v^* was calculated from the measured tangential velocity component u^* by integrating the continuity equation $\nabla^* \cdot \mathbf{u}^* = 0$. The

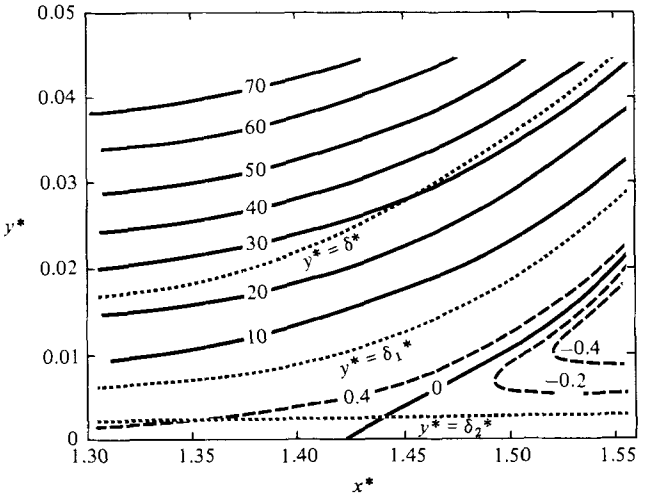

FIGURE 6. Streamlines; values of $1000\psi^*$ are given.

continuity equation was first expressed in the polar coordinate system (r^*, θ) and then the substitutions $r^* = 1 + y^*$ and $x^* = \theta$ were made, giving

$$\frac{\partial u^*}{\partial x} + \frac{\partial}{\partial y^*}[(1+y^*)\,v^*] = 0,$$

which was integrated numerically to give v^*. The streamlines of the flow shown in figure 6 were obtained by numerical integration of

$$u^* = \frac{\partial \psi^*}{\partial y^*},$$

where ψ^* is the stream function. The isovorticity lines (figure 7) of the flow were obtained by numerical differentiation using the equation

$$\omega^* = \frac{1}{1+y^*}\left\{\frac{\partial v^*}{\partial x^*} - \frac{\partial}{\partial y^*}[(1+y^*)\,u^*]\right\},$$

where ω^* is the vorticity.

4.2. *Comparison with flow properties deduced from the Navier–Stokes equations*

The measurements were checked against the properties of the curves $u^* = 0$, $\omega^* = 0$ and $\psi^* = 0$ which have been deduced from the Navier–Stokes equations. The angles subtended by these curves and the wall were $\alpha = 5.2°$, $\beta = 2.7°$ and $\gamma = 7.4°$ respectively. Legendre (1955) showed that $\tan\beta/\tan\gamma = \frac{1}{3}$. The observed value of 0.37 compares favourably with this. Oswatitsch (1958) showed that $\tan\alpha/\tan\gamma = \frac{2}{3}$. The observed value of 0.71 compares favourably with this. Oswatitsch also showed that

$$\tan\gamma = \frac{-3\dfrac{\mathrm{d}\tau_w}{\mathrm{d}x}(x_s)}{\dfrac{\mathrm{d}p_w}{\mathrm{d}x}(x_s)}.$$

These derivatives were calculated from the measured wall shear stress and wall pressure, and $\gamma = 4.4°$ was obtained. In contrast, the value obtained from the

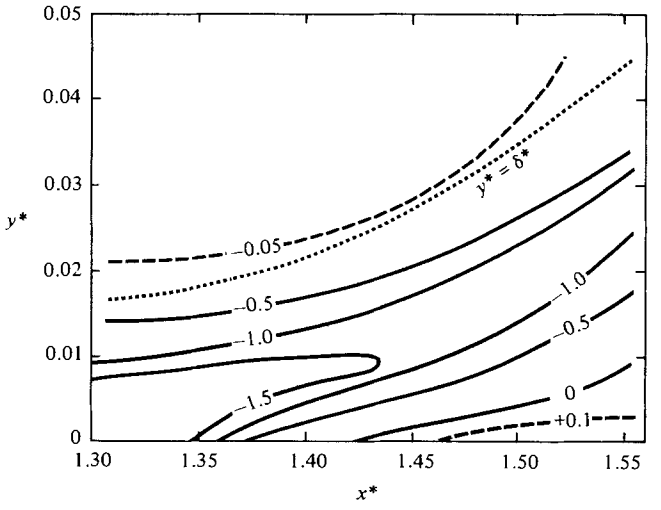

FIGURE 7. Isovorticity lines; values of $1000\omega^*$ are given. A counterclockwise rotation in the plane of figure 2 corresponds to a positive vorticity.

velocity measurements was $\gamma = 7.4°$ and the value obtained by flow visualization was $\gamma = 7°$. This difference was attributed mainly to the large uncertainty in the calculated pressure gradient $\mathrm{d}p_w/\mathrm{d}x$.

4.3. *Time-dependent behaviour of the flow*

Small variations in the flow with time were measured. Spectral analysis showed that the flow was not periodic, as would be the case if unsteady phenomena such as vortex shedding had occurred. Thus the flow was quasi-steady. The agreement between the data and the predictions of the Navier–Stokes equations suggests that the flow was essentially laminar.

4.4. *Approximation to the Navier–Stokes equations*

The most direct test of whether the boundary-layer equations apply to the flow in the neighbourhood of a separation point is the measurement of the individual terms in the Navier–Stokes equations to determine which terms are negligible. This test was made.

The Navier–Stokes equations

$$(\boldsymbol{u}\cdot\nabla)\,\boldsymbol{u} = -\frac{1}{\rho}\nabla p + \nu\nabla^2\boldsymbol{u},$$

were written in wall coordinates (x^*, y^*). The x^* momentum equation is

$$\begin{aligned}\frac{u^*}{1+y^*}\frac{\partial u^*}{\partial x^*} + v^*\frac{\partial u^*}{\partial y^*} + \frac{u^*v^*}{1+y^*} &= -\frac{1}{1+y^*}\frac{\partial p^*}{\partial x^*} + \frac{1}{Re}\frac{1}{(1+y^*)^2}\frac{\partial^2 u^*}{\partial x^{*2}} + \frac{1}{Re}\frac{\partial^2 u^*}{\partial y^{*2}} \\ &\quad + \frac{1}{Re}\frac{1}{1+y^*}\frac{\partial u^*}{\partial y^*} + \frac{1}{Re}\frac{2}{(1+y^*)^2}\frac{\partial v^*}{\partial x^*} - \frac{1}{Re}\frac{u^*}{(1+y^*)^2}, \end{aligned} \tag{1a}$$

and the y^* momentum equation is

$$\frac{u^*}{1+y^*}\frac{\partial v^*}{\partial x^*}+v^*\frac{\partial v^*}{\partial y^*}-\frac{u^{*2}}{1+y^*}=-\frac{\partial p^*}{\partial y^*}+\frac{1}{Re}\frac{1}{(1+y^*)^2}\frac{\partial^2 v^*}{\partial x^{*2}}+\frac{1}{Re}\frac{\partial^2 v^*}{\partial y^{*2}}$$
$$+\frac{1}{Re}\frac{1}{1+y^*}\frac{\partial v^*}{\partial y^*}-\frac{1}{Re}\frac{v^{*2}}{(1+y^*)^2}-\frac{1}{Re}\frac{2}{(1+y^*)^2}\frac{\partial u^*}{\partial x^*}, \tag{1b}$$

where $Re = U_\infty R/\nu$ is the Reynolds number based on the cylinder radius. Without considering the pressure derivatives, there are 16 terms in (1*a*, *b*). Many of the terms in (1*a*, *b*) proved to be extremely small, so that these equations were accurately approximated by the simpler forms

$$\frac{u^*}{1+y^*}\frac{\partial u^*}{\partial x^*}+v^*\frac{\partial u^*}{\partial y^*}+\frac{u^*y^*}{1+y^*}=-\frac{1}{1+y^*}\frac{\partial p^*}{\partial x^*}+\frac{1}{Re}\frac{\partial^2 u^*}{\partial y^{*2}}, \tag{2a}$$

$$\frac{u^*}{1+y^*}\frac{\partial v^*}{\partial x^*}+v^*\frac{\partial v^*}{\partial y^*}-\frac{u^{*2}}{1+y^*}=-\frac{\partial y^*}{\partial y^*}+\frac{1}{Re}\frac{\partial^2 v^*}{\partial y^{*2}}. \tag{2b}$$

Representative profiles of the velocity terms in (2*a*, *b*) are shown in figures 8–10. The trend of the data was visualized by fairing lines through the data points. Their shape is not known with high accuracy because of the scatter in the data.

Many of the terms appearing in (2*a*, *b*) are negligible within certain regions of the flow. For example, the second-derivative terms, which represent viscous effects, are negligible for $y^* > \delta_1^*$.

Within the displacement thickness of the boundary layer ($y^* < \delta_1^*$), the complete Navier–Stokes equations were approximated by the equations

$$u^*\frac{\partial u^*}{\partial x^*}+v^*\frac{\partial u^*}{\partial y^*}=-\frac{\partial p^*}{\partial x^*}+\frac{1}{Re}\frac{\partial^2 u^*}{\partial y^{*2}}, \tag{3a}$$

$$0=-\frac{\partial p^*}{\partial y^*}, \tag{3b}$$

with an error of less than 10%. The $1+y^*$ factors have been dropped in accordance with this level of approximation. Equations (3*a*, *b*) are the classical boundary-layer equations.

Outside the displacement thickness of the boundary layer ($y^* \geqslant \delta_1^*$), the complete Navier–Stokes equations are approximated by the equations

$$\frac{u^*}{1+y^*}\frac{\partial u^*}{\partial x^*}+v^*\frac{\partial u^*}{\partial y^*}+\frac{u^*v^*}{1+y^*}=-\frac{1}{1+y^*}\frac{\partial p^*}{\partial x^*}, \tag{4a}$$

$$\frac{u^*}{1+y^*}\frac{\partial v^*}{\partial x^*}+v^*\frac{\partial v^*}{\partial y^*}-\frac{u^{*2}}{1+y^*}=-\frac{\partial p^*}{\partial y^*}, \tag{4b}$$

with an error of less than 10%. The effects of coordinate-system curvature are retained in these equations. Equations (4*a*, *b*) are the Euler equations for inviscid flow.

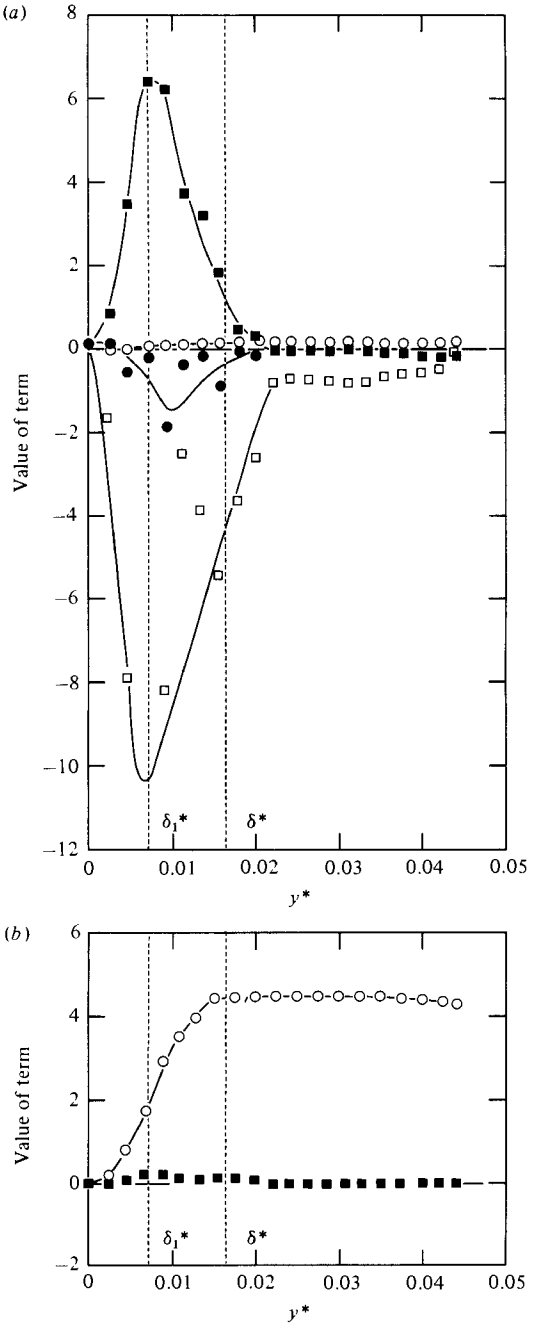

FIGURE 8. Terms in the momentum equations at $\theta = 75.0°$:

(*a*) □, $\dfrac{u^*}{1+y^*}\dfrac{\partial u^*}{\partial x^*}$; ■, $v^*\dfrac{\partial u^*}{\partial y^*}$; ○, $\dfrac{u^*v^*}{1+y^*}$; ●, $\dfrac{1}{Re}\dfrac{\partial^2 u^*}{\partial y^{*2}}$;

(*b*) □, $\dfrac{u^*}{1+y^*}\dfrac{\partial v^*}{\partial x^*}$; ■, $v^*\dfrac{\partial v^*}{\partial y^*}$; ○, $\dfrac{u^{*2}}{1+y^*}$; ●, $\dfrac{1}{Re}\dfrac{\partial^2 v^*}{\partial y^{*2}}$.

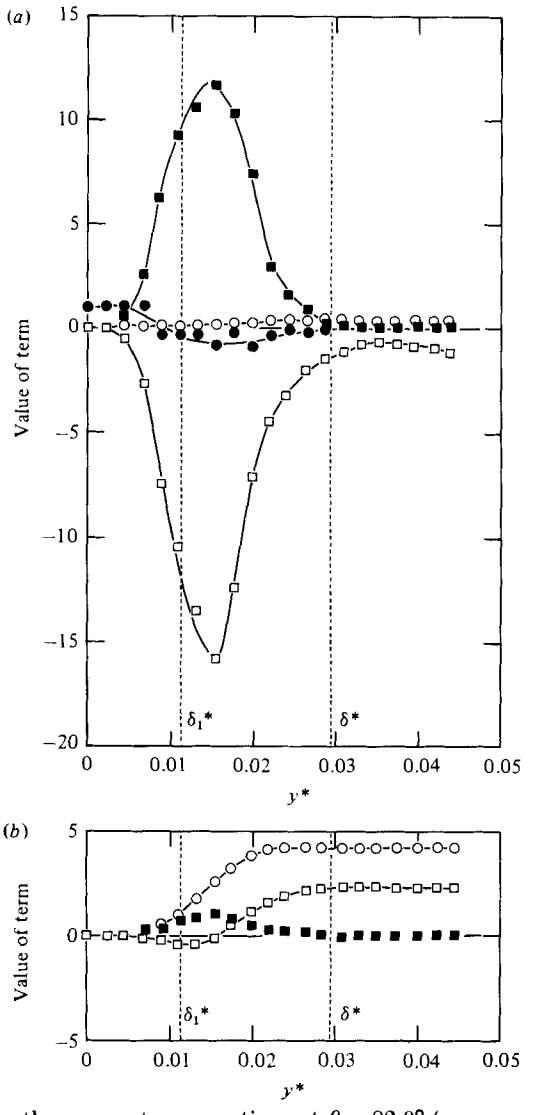

FIGURE 9. Terms in the momentum equations at $\theta = 82.0°$ (same symbols as figure 8).

The validity of (3) and (4) is suggested by comparison of the absolute values of the profiles shown in figures 8–10. To simplify analysis of the data, a function

$$f_i(x,y) = \frac{a_i(x,y)}{\max\limits_{i=1,2,\ldots,16} a_i(x,y)}$$

was calculated, where $a_i(x,y)$ is the absolute value of the ith velocity term in (1a, b). The values of $f_i(x,y)$ measure the importance of each term.

Since there is an experimental uncertainty in u^*, x^* and y^*, there is an uncertainty in all derived values. The uncertainty in each term at each mesh point was estimated by repeating the entire calculation using a value of $u^* \pm \Delta u^*$, where Δu^* is the uncertainty in u^* and the sign is chosen randomly at each mesh point. The effects

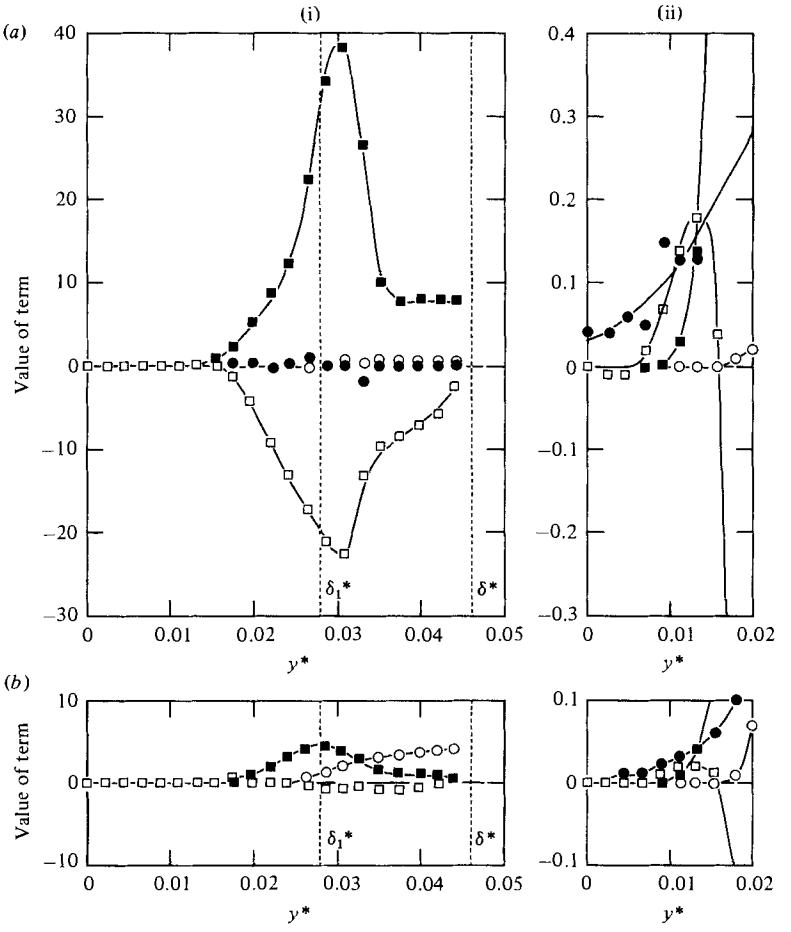

FIGURE 10. Terms in the momentum equations at $\theta = 89.0°$ (same symbols as figure 8).

of the uncertainty in x^* and y^* were negligible by comparison. The estimated uncertainty in the values of $f_i(x, y)$ was less than 0.1 in all cases.

These results suggest that the edge of the displacement thickness ($y^* = \delta_1^*$) divides the flow into an inner region where the boundary-layer equations apply and an outer region where the Euler equations apply. This role is more often given to the edge of the boundary layer ($y^* = \delta^*$) in boundary-layer calculations, but using the displacement thickness is also reasonable because of the asymptotic nature of boundary-layer theory.

4.5. *Pressure distribution*

From the Navier–Stokes equations,

$$\frac{\partial p^*}{\partial x^*}(x^*, 0) = \frac{1}{Re}\frac{\partial^2 u^*}{\partial y^{*2}}(x^*, 0).$$

Using the velocity measurements, this equation was numerically integrated to give the wall pressure distribution. The calculated and measured wall-pressure distributions are shown in figure 5. The constant of integration was chosen to move the calculated curve into coincidence with the measured curve. The two curves agreed well, except

near $\theta = 75°$ where the velocity could not be accurately differentiated. This comparison provided a check of the measurements.

The pressure gradient $\partial p^*/\partial y^*$ was calculated from the measured velocity using (1*b*) and was then integrated, giving the pressure change across the boundary layer. The pressure change $|p^* - p_w^*|$ was less than 0.02 within the displacement thickness and less than 0.04 within the remainder of the boundary layer. This demonstrates again that the boundary-layer equations apply within the displacement thickness.

5. Comparison with other work

The experimental results have shown that the boundary-layer equations are valid in the neighbourhood of the separation point. This and other measured properties of the flow will now be used to examine the validity of some proposed theories for a separation point.

5.1. *Comparison with solutions of the boundary-layer equations using a pressure or velocity boundary condition*

The wall-shear-stress distribution shown in figure 4 was described by

$$\tau_w^* = k(x_s^* - x^*)^n,$$

where $k = 0.042 \pm 0.014$, $n = 1.15 \pm 0.14$ and $0 \leqslant x_s^* - x^* \leqslant 0.1$. Therefore solutions for which $\mathrm{d}\tau_w^*/\mathrm{d}x^*$ is infinite, such as that of Goldstein (1948), are not applicable.

Messiter & Enlow (1973) found a solution to the boundary-layer equations, which is regular at the separation point. They required that $\mathrm{d}P^*/\mathrm{d}x^* < 0$ for $x^* < x_s^*$, where P^* is the pressure at the edge of the boundary layer. This assumption does not apply to the pressure distribution shown in figure 5.

Sychev (1974) concluded that there is an abrupt increase of $\mathrm{d}P^*/\mathrm{d}x^*$ in a measurable neighbourhood of the separation point. This was not observed in the pressure distribution shown in figure 5.

It is widely believed that the flow in the neighbourhood of a separation point is very sensitive to the pressure or velocity at the edge of the boundary layer (see e.g. Leal 1973). It may be that solutions of the boundary-layer equations using a pressure or velocity boundary condition have failed because the prescribed boundary condition was physically unrealistic. It is not apparent from the present measurements what the correct boundary condition should be.

5.2. *Comparison with solutions of the boundary-layer equations using inverse boundary conditions*

Catherall & Mangler (1966) used the following inverse method. The velocity distribution $q(x)$ on the displacement surface $y = \delta_1(x)$ was prescribed until near $x = x_s$, then the displacement surface $y = \delta_1(x)$ was prescribed for $x \approx x_s$. The flow outside the displacement surface was considered inviscid and the flow within it was assumed to obey the boundary-layer equations. This choice of governing equations and the region in which they apply is supported by the experimental data. The measured flow field agreed qualitatively with their solution.

Carter (1975) used two inverse techniques: prescribed displacement thickness and prescribed wall shear stress. The measured flow field agreed qualitatively with Carter's solution near the separation point.

5.3. *Comparison with other theories*

The measured pressure distribution satisfied the necessary condition for the existence of a solution of the boundary-layer equations that is regular at the separation point, as proposed by Meksyn (1961). This condition is satisfied because of the change of slope of the pressure distribution near the separation point, which is shown in figure 5.

The angle subtended by the separation streamline and the wall agrees with the flow-visualization study of Dobbinga, van Ingen & Kooi (1972).

6. Conclusion

The main conclusion of this study is that the boundary-layer equations are valid at, and near, a separation point in a steady laminar flow at a high subcritical Reynolds number.

The existence of singular solutions of the boundary-layer equations at separation, when a prescribed pressure or velocity boundary condition is used, had suggested that the boundary-layer equations were not valid in the neighbourhood of the separation point. Inverse boundary conditions had permitted non-singular solutions of the boundary-layer equations, but they had not been experimentally tested. The experiments described in this paper provided direct support for the boundary-layer equations in the neighbourhood of the separation point and indicated that inverse solutions are valid there.

The authors gratefully acknowledge the support of the Natural Sciences and Engineering Research Council of Canada for supporting this work through grant A3806. This work was originally part of a thesis at the University of Toronto (Varty 1980).

REFERENCES

Brown, S. N. & Stewartson, K. 1969 Laminar separation. *Ann. Rev. Fluid Mech.* **1**, 45–72.

Carter, J. E. 1975 Inverse solutions for laminar boundary-layer flows with separation and reattachment. *NASA* TR-R447.

Catherall, D. & Mangler, K. W. 1966 The integration of the two-dimensional laminar boundary-layer equations past the point of vanishing skin friction. *J. Fluid Mech.* **26**, 163–182.

Dobbinga, E., van Ingen, J. L. & Kooi, J. W. 1972 Some research on two dimensional laminar separation bubbles. Dept Aero. Engng, Technological University of Delft, The Netherlands.

Durst, F., Melling, A. & Whitelaw, J. H. 1976 *Principles and Practice of Laser Anemometry.* Academic.

Goldstein, S. 1948 On laminar boundary-layer flow near a position of separation. *Q. J. Mech. Appl. Maths* **1**, 43–69.

Leal, L. G. 1973 Steady separated flow in a linearly decelerated free stream. *J. Fluid Mech.* **59**, 513–535.

Legendre, R. 1955 Mécanique des fluides visqueux-décollement laminaire régulier. *C.R. Acad. Sci. Paris* **241**, 732–734.

Meksyn, D. 1961 *New Methods in Laminar Boundary-Layer Theory.* Pergamon.

Messiter, A. F. & Enlow, R. L. 1973 A model for laminar boundary flow near a separation point. *SIAM J. Appl. Maths* **25**, 655–670.

Oswatitsch, K. 1958 Die Ablösungsbedingung von Grenzschichten. In *Proc. IUTAM Symp. on Boundary-Layer Research*, 1957 (ed. H. Görtler), pp. 357–367.

SYCHEV, V. V. 1974 Laminar separation. *Fluid Dyn.* **7**, 407–417.

TILLMAN, W. & SCHLIEPER, H. 1979*a* Modification of miniature flush surface wall shear probes for biomedical use. *J. Phys.* E: *Sci. Instrum.* **12**, 371–372.

TILLMAN, W. & SCHLIEPER, H. 1979*b* A device for the calibration of hot-film wall shear probes in liquids. *J. Phys.* E: *Sci. Instrum.* **12**, 373–380.

VARTY, R. L. 1980 An experimental study of a laminar separation point. Ph.D. thesis, University of Toronto.

WILLIAMS, J. C. 1977 Incompressible boundary-layer separation. *Ann. Rev. Fluid Mech.* **9**, 113–144.